

JGR Space Physics

TECHNICAL REPORTS: METHODS

10.1029/2019JA026910

Key Points:

- A proof-of-concept study for assimilating satellite far ultraviolet observations of dayglow using an ensemble filter is presented
- Observing system simulation experiments assess the impact of GOLD observations on thermospheric temperature specification
- Experiments result in considerable reduction of modeled temperature bias under geomagnetically quiet and moderately disturbed conditions

Correspondence to:

C. E. Cantrall,
clayton.cantrall@colorado.edu

Citation:

Cantrall, C. E., Matsuo, T., & Solomon, S. C. (2019). Upper atmosphere radiance data assimilation: A feasibility study for GOLD far ultraviolet observations. *Journal of Geophysical Research: Space Physics*, 124, 8154–8164. <https://doi.org/10.1029/2019JA026910>

Received 2 MAY 2019

Accepted 25 SEP 2019

Accepted article online 12 OCT 2019

Published online 30 OCT 2019

©2019. The Authors.

This is an open access article under the terms of the Creative Commons Attribution License, which permits use, distribution and reproduction in any medium, provided the original work is properly cited.

Upper Atmosphere Radiance Data Assimilation: A Feasibility Study for GOLD Far Ultraviolet Observations

Clayton E. Cantrall¹ , Tomoko Matsuo¹ , and Stanley C. Solomon² 

¹Department of Aerospace Engineering Sciences, University of Colorado, Boulder, CO, USA, ²High Altitude Observatory, National Center for Atmospheric Research, Boulder, CO, USA

Abstract Far ultraviolet observations of Earth's dayglow from the National Aeronautics and Space Administration (NASA) Global-scale Observations of the Limb and Disk (GOLD) mission presents an unparalleled opportunity for upper atmosphere radiance data assimilation. Assimilation of the Lyman-Birge-Hopfield (LBH) band emissions can be formulated in a similar fashion to lower atmosphere radiance data assimilation approaches. To provide a proof-of-concept for such an approach, this paper presents assimilation experiments of simulated LBH emission data using an ensemble filter measurement update step implemented with National Oceanic and Atmospheric Administration (NOAA)'s Whole Atmosphere Model (WAM) and National Center for Atmospheric Research (NCAR)'s Global Airglow (GLOW) model. Primary findings from observing system simulation experiments (OSSEs), wherein “truth” atmospheric conditions simulated by NCAR's Thermosphere Ionosphere Electrodynamics General Circulation Model (TIEGCM) are used to generate synthetic GOLD data, are as follows: (1) Assimilation of GOLD LBH disk emission data can reduce the bias in model temperature specification (ensemble mean) by 60% under both geomagnetically quiet conditions and disturbed conditions. (2) The reduction in model uncertainty (ensemble spread) as a result of assimilation is about 20% in the lower thermosphere and 30% in the upper thermosphere for both conditions. These OSSEs demonstrate the potential for far ultraviolet radiance data assimilation to dramatically reduce the model biases in thermospheric temperature specification and to extend the utility of GOLD observations by helping to resolve the altitude-dependent global-scale response of the thermosphere to geomagnetic storms.

1. Introduction

The Earth's thermosphere is driven by highly variable forcing from the Sun and from the lower atmosphere. Most notably, observations have revealed a considerable contribution of wave forcing from the lower atmosphere to the day-to-day variability of the upper atmosphere (e.g., Lin et al., 2007). In conjunction with observational evidences, whole atmosphere models have successfully reproduced variability in the thermosphere and ionosphere as a result of the wave forcing from the various lower atmosphere sources (e.g., Fang et al., 2013; Liu et al., 2013). The thermosphere's day-to-day variability in response to variable forcing is not completely understood. Our lack of understanding is most apparent when comparing model responses to observed responses during large events, such as Sudden Stratospheric Warmings and geomagnetic storms. The limited knowledge of the thermosphere's response to external forcing is due in part to past observations of this atmospheric region having confined spatial and temporal coverages.

Satellite-based far ultraviolet (FUV) remote sensing has proven to be a valuable technique for monitoring thermospheric variables over large spatial areas. FUV remote sensing missions that have used the LBH bands include the Polar satellite's Ultraviolet Imager (UVI; 1996–2008), the Advanced Research and Global Observation Satellite's (ARGOS) High Resolution Ionospheric and Thermospheric Spectrograph (HITS; 1999–2003), the Thermosphere-Ionosphere-Mesosphere Energetics and Dynamics (TIMED) satellite's Global Ultraviolet Imager (GUVI; 2001–present), and the Defense Meteorological Satellite Program (DMSP) Special Sensor Ultraviolet Spectrographic Imager (SUSSI; 2003–present). These missions have brought on important discoveries into the thermospheric response to changes in lower atmosphere and solar and magnetosphere conditions (Dymond et al., 1999; Meier et al., 2015; Paxton et al., 1992; Torr

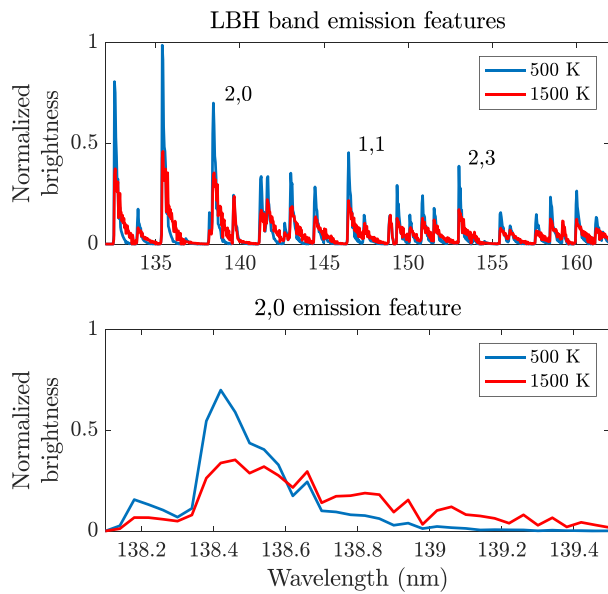


Figure 1. (a) Simulated N_2 Lyman-Birge-Hopfield (LBH) emissions between the GOLD bandwidth of 132–162 nm at two temperatures. The specified (2,0), (1,1), and (2,3) vibrational transitions are those assimilated. (b) The temperature dependence is observed by the effective skewing of the (2,0) feature with increased temperature due to increased occupancy of rotational energy levels. The wavelengths longer than 138.6 nm are positively correlated with temperature and those shorter are negatively correlated.

et al., 1995). However, the orbital constraints and/or the spectral resolution of the instruments restricted these missions from monitoring the temporal evolution of temperature changes on a global-scale. If temperature structure, which affects thermospheric winds and compositions, is only known in confined areas, the overall thermospheric dynamics is under-constrained. This ultimately limits the ability to unravel intricate coupling processes taking place in the thermosphere and ionosphere during times of elevated forcing.

The Global-scale Observations of the Limb and Disk (GOLD) mission will help address the lack of global thermospheric temperature measurements by continuously monitoring the daytime N_2 Lyman-Birge-Hopfield (LBH) band emissions between 132 and 162 nm over Earth's disk at a fine spectral resolution (Eastes et al., 2017). Budzien et al. (2001) and Aksnes et al. (2006) demonstrated the neutral temperature of the lower thermosphere (~160–270 km) can be retrieved from the shape of the LBH band features that relates to the N_2 rotational structure using HITS data. The shape of the band features is effectively skewed to longer wavelengths with an increase in the rotational temperature of the molecule (one-to-one relationship between the rotational and neutral temperature) that results in the population of higher rotational levels (shown in Figure 1). A thorough discussion of the LBH temperature dependence and the relationship between the neutral and rotational temperatures is provided in Aksnes et al. (2006). Eastes et al. (2011) used HITS to show that an LBH temperature retrieval has the precision to observe atmospheric tides and gravity waves across the thermosphere. These studies paved the way for probing thermospheric temperature on the limb and disk through space-based ultraviolet remote sensing.

Data assimilation is the process of combining observations with a numerical forecast model of a geophysical system and is a powerful tool in specifying and forecasting highly dynamical systems like Earth's thermosphere. Ensemble filters can handle a nonlinear forward model that converts the model state variables to observed variables without requiring a corresponding adjoint operator. In particular, variants of ensemble square root filters (EnSRFs; e.g., Tippett et al., 2003) have been widely used in atmospheric and oceanic data assimilation applications (Anderson, 2001; Bishop et al., 2001 and Whitaker & Hamill, 2002) including National Oceanic and Atmospheric Administration (NOAA)'s operational numerical weather prediction systems (Whitaker et al., 2008). EnSRFs have also proven to be a valuable technique for assimilating thermospheric and ionospheric observations into thermosphere and ionosphere models (e.g., Lee et al., 2012; Matsuo et al., 2012). This paper presents a proof-of-concept study for upper atmosphere radiance data assimilation using an EnSRF measurement-update step implemented with NOAA's Whole Atmosphere Model (WAM; Akmaev, 2011) as the numerical forecast model and National Center for Atmospheric Research (NCAR)'s Global Airglow (GLOW) model (Solomon, 2017) as part of the forward model. The formulation follows a commonly used data assimilation practice of directly assimilating radiances instead of a retrieval product as it is less prone to introducing errors and biases due to inconsistency between the retrieval process and data assimilation scheme.

The quality of dayside temperature estimates from 100 to 500 km altitudes resulting from assimilation of GOLD LBH disk emission data is assessed using observing system simulation experiments (OSSEs). OSSEs provide a quantitative evaluation of the impacts that a given observing system will have on specification and forecasting of geophysical conditions and can also be used to test the performance of a data assimilation system. In OSSEs, synthetic observations, generated from a "truth" state, are assimilated and the state estimates by data assimilation are compared against the truth state. In this study, the truth thermospheric conditions are simulated by NCAR's Thermosphere Ionosphere Electrodynamics General Circulation Model (TIEGCM; Qian et al., 2014; Richmond et al., 1992) from which synthetic GOLD LBH disk emission data are generated as described later. Note that synthetic GOLD LBH disk emission data are equivalent to the GOLD Level 1C radiance data product.

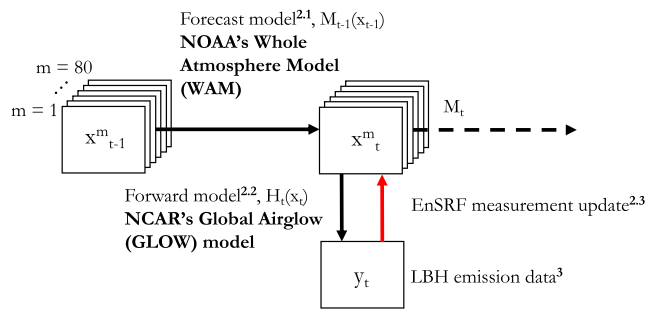


Figure 2. Diagram of the ensemble square root filter (EnSRF) data assimilation design. Data assimilation is implemented as an iterative two-step process with a forecast and measurement update. The focus of this study is on the measurement update denoted by the red arrow. The superscripts denote the section that describe each component.

Following this introduction, section 2 covers the data assimilation system design and section 3 covers synthetic observations for the OSSEs. In section 4, we examine the data assimilation performance under different magnetospheric forcing conditions.

2. Data Assimilation System Design

Data assimilation is typically implemented as a recursive process of a state forecasting step and a measurement update as summarized in Figure 2 for an ensemble filter with m ensemble members. A forecast model M_t provides the prior knowledge of the state x at time t . If an observation y is available at time t , the forecasted state is mapped to observation space via a forward model H_t . This forward model is effectively inverted as part of ensemble filter processes to obtain the measurement-updated state at time t as shown by the red arrow in Figure 2. After this measurement update step, a new forecast is launched from the updated model states.

For the purpose of demonstrating the effectiveness of an upper atmosphere radiance data assimilation approach, this paper focuses only on a single measurement-update step and thus the t subscript is dropped for remainder of the paper. Furthermore, the measurement at each GOLD pixel is assumed to be dependent only on the atmospheric column defined by the pixel size. This is a reasonable assumption because multiple scattering in the thermosphere is negligible compared to the rate of excitation and absorption of LBH emission. The temperature estimation problem is then simplified to one spatial dimension, where the thermospheric column-integrated LBH spectrum measured at each pixel (observation y) is used to update temperature x at h discrete altitude levels along the line-of-sight.

Sections 2.1 and 2.2 describe the forecast model and forward model in detail; the two main components of the data assimilation system used for this study. Section 2.3 describes specific steps of the implemented ensemble filter algorithm.

2.1. Forecast Model and WAM Ensemble Simulation

The version of WAM coupled with the Global Ionosphere Plasmasphere model described in Fang et al. (2018) is used to generate an ensemble of the whole atmosphere simulations. The simulations ran under nominal conditions of January 2012 ($F_{10.7} = 141$ sfu) using the 5-min solar wind and interplanetary magnetic field and daily solar irradiance data. The effects of solar UV and EUV irradiance variability are parameterized with the 22 EUV and 15 UV spectral bands of Solomon and Qian (2005) using SDO/EVE and TIMED/SEE NASA data from 2011 to 2012. The across-band and temporal correlation structures of the 37 spectral bands are evaluated to build a stochastic perturbation model for the solar UV and EUV forcing. Suppose $F^i(s)$ represents the solar EUV irradiance [photons/cm²/s] for a given spectral bin s for the i^{th} ensemble member simulation:

$$F^i(s) = \bar{F}(s) + F'^i(s) \quad i = 1, \dots, m$$

where $\bar{F}(s)$ is the daily mean value, $F'^i(s)$ is a stochastic component randomly drawn from the centered multivariate normal distribution for each member, i . Note that $F'^i(s)$ reflects the across-band and temporal correlation structures found in SDO/EVE and TIMED/SEE data. The m -member ensemble simulation of WAM $\{x^1, \dots, x^m\}$ is initialized by corresponding specification of the UV and EUV flux from the m -member ensemble of the UV and EUV forcing specification $\{F^1, \dots, F^m\}$.

2.2. Forward Model and GOLD Measurements

GOLD measures ultraviolet radiances between 132 and 162 nm from a geostationary orbit over South America at 47.5°W longitude. Full coverage of Earth's disk is provided at a cadence of 30 min. The spatial resolution at nadir is expected to be 125 × 125 km, and the spectral resolution is 0.04 or 0.08 nm depending on the entrance slit.

The data assimilation requires a forward model operator that maps the model state, x , to GOLD measurements, y :

$$y = H(x) + \epsilon$$

where ϵ is the observational error, normally distributed with covariance R centered at zero. This observational error includes effects of measurement errors and representativeness errors originating from forward modeling. The forward model operator, H , has been implemented by using the NCAR GLOW model and a radiative transfer model (Solomon, 2017). The GLOW model calculates thermospheric volume emission rates in the FUV on the 3-dimensional (altitude, latitude, and longitude) grid, which are input to the radiative transfer model to produce thermospheric column-integrated radiances at the GOLD spatial and spectral resolution on a two-dimensional (latitude, longitude) grid. This radiative transfer model contains the LBH band model (Budzien et al., 2001), which calculates the LBH synthetic spectrum using available laboratory-based molecular data (e.g., Huber & Herzberg, 1979). The nonlinear dependence of the LBH emission on temperature is primarily determined by the LBH band model. Another possible source of nonlinear temperature dependence is the O_2 photo-absorption cross section (Lean & Blake, 1981), which is mostly negligible over the temperature and wavelength range of interest. An ensemble data assimilation approach enables us to account for the realistic non-local and nonlinear temperature dependence of LBH emissions when assimilating the GOLD measurements.

The radiances computed from radiative transfer are then converted to photon counts based on the throughput efficiencies over bandwidth, integration time, geometry of the pixel, spatial binning, and the full-width-half-maximum wavelength resolution. These photon counts are equivalent to the GOLD Level 1C radiance data product. A specific observation type used as y in this study is a ratio between the “short” and “long” spectral counts of an LBH emission feature observed by GOLD. The ratio is a first-order approximation of the shape of the emission feature, which contains the temperature information. Referring to the (2,0) vibrational transition feature shown in Figure 1b, the “short” spectral bins are those below 138.6 nm and the “long” spectral bins are those above 138.6 nm for the (2,0) emission feature. The counts in the short and long spectral bins generally have a negative and positive correlation with temperature, respectively. Similarly, the (1,1) features spans ~146.4–147.2 nm with a long to “short threshold wavelength of 146.65 nm and the (2,3) feature spans ~153.0–153.7 nm with a threshold wavelength of 153.25 nm. The mean ratio derived from these three emission features labeled in Figure 1a is assimilated as observation y . Note that the short and long spectral distinction adopted in this study does not correspond to the GUVI “LBH short” and “LBH long” broad spectral band distinction.

2.3. Ensemble Square Root Filter Measurement Update

The EnSRF presents a low-rank approximation of the conventional Kalman filter, which uses sample statistics from an ensemble of model forecasts to determine the impact that observations have on the data assimilation update of model state variables. The ensemble transform implementation follows that of Anderson (2003). This ensemble transform is performed for each pixel of GOLD disk emission data.

Important components of the ensemble transform are two sets of ensemble: the forecast (prior) model ensemble $\{x_f^1, \dots, x_f^m\}$ and forecast observation ensemble $\{y_f^1, \dots, y_f^m\}$. NOAA's WAM is used to generate the forecast model ensemble $\{x_f^1, \dots, x_f^m\}$ as described in section 2.1. x is a vector of size h corresponding to temperature at h discrete pressure levels. The mean of the forecast model ensemble \bar{x}_f is the best estimate of the temperature by the forecast. The forecast observation ensemble $\{y_f^1, \dots, y_f^m\}$ is computed by applying forward modeling of the GOLD measurement to each ensemble member $\{x_f^1, \dots, x_f^m\}$ as described in section 2.2.

The covariance P of x is approximated by the m -member ensemble $\{x^1, \dots, x^m\}$ as follows. Note that the rank of P is at most $m - 1$ and $h > m$.

$$P \approx D_x D_x^T$$

$$D_x = \frac{1}{\sqrt{m-1}} [[x^1], \dots, [x^m]]$$

where the matrix D_x is composed of the mean-subtracted temperature of the i th ensemble member ($x^i = x^i - \bar{x}$). In the update step, the forecast ensemble is transformed into the measurement-updated (posterior) ensemble, such that the sample statistics of the measurement-updated ensemble for the mean and covariance is consistent with what are expected by the Kalman measurement update equations.

The specific implementation to compute the measurement-updated ensemble when an observation is available is as follows:

1. Create the $h \times m$ data matrices D_x and D_y as

$$D_x = \frac{1}{\sqrt{m-1}} \left[[x_f^1], \dots, [x_f^m] \right]$$

$$D_y = \frac{1}{\sqrt{m-1}} \left[[y_f^1], \dots, [y_f^m] \right]$$

2. Update the ensemble mean using observation y_j ($j = 1, \dots, k$), with its error variance R_{jj} in observation space:

$$\bar{y}_{aj} = \bar{y}_{fj} + \frac{D_{y_j} D_{y_j}^T}{D_{y_j} D_{y_j}^T + R_{jj}} (y_j - \bar{y}_{fj})$$

3. Update each ensemble member ($i = 1, \dots, m$)

$$y_{aj}^i = \sqrt{\frac{R_{jj}}{R_{jj} + D_{y_j} D_{y_j}^T}} (y_{fj}^i - \bar{y}_{fj}) + \bar{y}_{aj}$$

4. Update each ensemble member in state space

$$x_{aj}^i = x_{fj}^i + \frac{D_x D_{y_j}^T}{D_{y_j} D_{y_j}^T} (y_{aj}^i - y_{fj}^i)$$

5. Repeat Steps 1–4 for each observation $y_1, y_2, \dots, y_j, \dots, y_k$ that corresponds to each pixel of GOLD disk emission data ($k = 10,000$ in this study for an 100×100 grid). The measurement-updated ensemble mean \bar{x}_a serves as the new best estimate of the state.

3. Synthetic Observation and Observing System Simulation Experiments

The NCAR TIEGCM is used to simulate the truth state of the thermosphere. Synthetic GOLD observations are produced by applying the forward model to the TIEGCM model outputs $H(x_{\text{truth}})$ as described in section 2.2. Note that the geostationary position of the satellite for these OSSEs is not set in the exact GOLD position, but the local-time distributions and line-of-sight geometry of GOLD data are properly taken into account in generating synthetic GOLD observations. In order to model the observation error R required for the data assimilation, effects of counting statistics are included in the forward model only when defining the synthetic observations. Counting statistics are the dominant noise source in the Level 1C data, modeled by a Poisson distribution with a mean that is set to the calculated photon counts for each pixel and spectral bin. R is specified by using the variance of these distributions.

Two OSSEs were conducted on 20 January 2012 at 6 UT under nominal conditions with two different levels of geomagnetic activity but at the same level of solar EUV conditions with a focus on the dayside thermosphere. TIEGCM simulations are ran for a time of quiet and moderately disturbed geomagnetic conditions with the same $F_{10.7} = 141$. The moderately disturbed conditions were generated by setting cross-tail potential = 120 kV and hemispheric power = 90 GW compared to cross-tail potential = 20 kV and hemispheric power = 14 GW for the quiet time simulation within the TIEGCM model. The WAM ensemble generated by perturbing solar UV and EUV forcing as described in section 2.1 for 20 January 2012 conditions was used for both OSSEs. Note that both TIEGCM simulations are biased from the WAM simulations with a larger bias for the disturbed time. The ensemble filter should be able to bring the WAM ensemble closer to the truth state and reduce the model bias if the data assimilation system is functioning as expected.

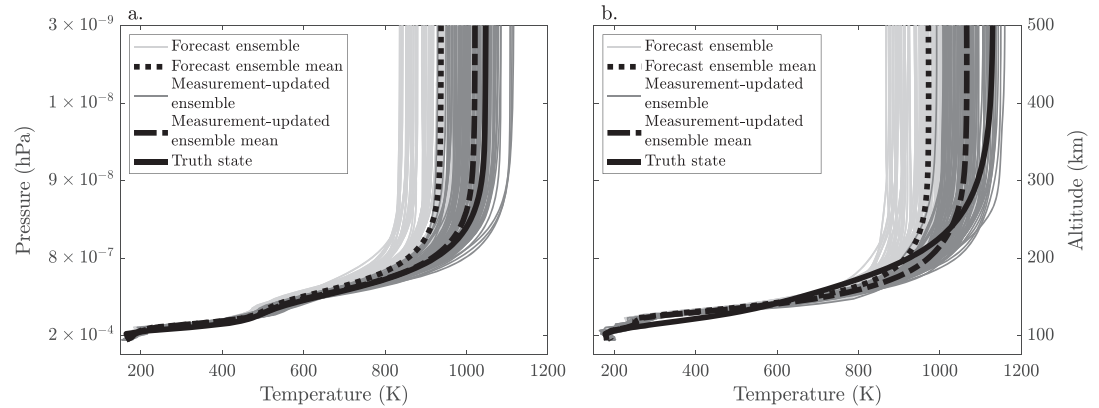


Figure 3. Example of temperature estimates in (a) the satellite's nadir direction and (b) near the limb. The solid black line represents the TIEGCM "truth" atmospheric temperature. The light gray lines are the WAM forecast ensemble members and the dotted line shows the ensemble mean (best estimate of temperature by WAM before data assimilation). The dark gray lines represent the measurement-updated ensemble after the observation has been assimilated with the dash line showing the ensemble mean (best estimate of temperature by WAM after data assimilation). See the labeled pixels in Figure 4 for the location of these temperature profiles on the disk.

The data assimilation time-window of 1 hr is adopted. In these OSSEs, the size of h is 100 corresponding to temperature at 100 pressure levels ranging from 100 to 500 km and the ensemble size m is 80.

4. Results

Accuracy of the data assimilation measurement-update obtained in the OSSE results can be interpreted in terms of the model bias or the difference between the WAM ensemble mean temperature and the TIEGCM truth atmosphere. The percent change in the model bias from the forecast to the measurement-update is computed as follows:

$$\Delta bias = 100 \times \frac{1}{hk} \sum_{l=1}^h \sum_{j=1}^k \frac{|\text{bias}(l,j)_a| - |\text{bias}(l,j)_f|}{|\text{bias}(l,j)_f|} \quad [\%]$$

where l is the l th pressure level out of h , j is the j th pixel out of k on the disk in GOLD's field-of-view, and $\text{bias}(l,j)_f$ and $\text{bias}(l,j)_a$ are the forecast and measurement-updated biases, respectively, at l,j . The precision (uncertainty) of the measurement-updated state can be represented by the standard deviation of the ensemble. If OSSEs are successfully, there is an increase in the model precision and a reduction in the ensemble spread after an observation has been assimilated. This is visualized in Figure 3, where the ensemble spread is decreased between the forecast ensemble (light gray) and measurement-updated ensemble (dark gray).

4.1. Quiet Time OSSE

Figure 3 provides a graphical representation of the measurement-update under quiet geomagnetic conditions in a single atmospheric column in the (a) nadir direction, and in a (b) near-limb direction. The location of these atmospheric columns in GOLD's field-of-view are denoted by black dots in Figure 4. In Figure 3a, there is a significant reduction in the modeled temperature bias after the forecast ensemble is transformed to the measurement-updated ensemble by the EnSRF measurement-update step. The maximum absolute measurement-updated bias is <10 K in the lower thermosphere at about 160 km altitude and 32 K in the upper thermosphere. In Figure 3b, it is evident that both the forecast and measurement updated temperature profile had difficulties capturing the temperature gradient in the lower thermosphere. While the temperature bias is reduced from forecast to measurement-update considering the entire profile, there is an increase in bias in the lower thermosphere (forecast bias of 51 K to measurement-update bias of 83 K at 160 km). This example highlights an inherent shortcoming of this under-determined inverse problem that is further discussed in section 5.

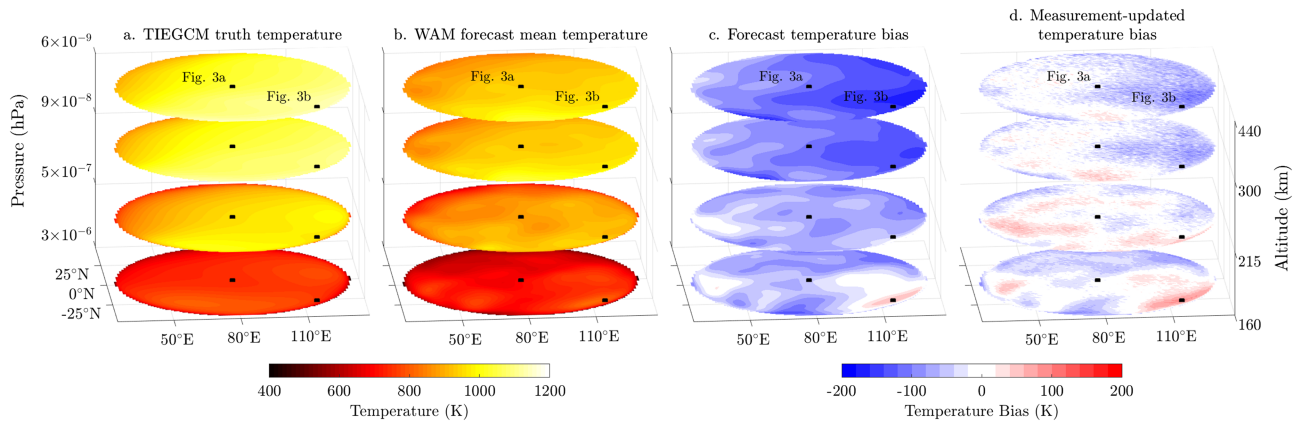


Figure 4. Three-dimensional plots showing (a) the TIEGCM “truth” atmospheric temperature, (b) the WAM forecast model predicted temperature, (c) the temperature bias between the “truth” temperature and forecast model, and (d) the temperature bias between the truth temperature and measurement-updated estimate after the observation has been assimilated. Figure 3 shows a graphical representation of the measurement update for the labeled pixels.

Figure 4 demonstrates effects of the measurement-update over the disk viewed by GOLD at four atmospheric pressure levels at around 160, 215, 300, and 440 km. Figures 4a and 4b show the temperature from the TIEGCM truth atmosphere and the WAM forecast ensemble mean, and Figures 4c and 4d display the bias in the atmospheric temperature before and after data assimilation. Comparing Figure 4c and Figure 4d, the measurement-update step generally reduces the model bias over the disk throughout the atmospheric layers. The white regions with the lowest temperature bias correspond to values between -20 and 20 K. The regions of maximum bias in the southeast limb of the disk correspond to absolute temperature differences of 110 K. The absolute mean temperature bias reduction from forecast to measurement-update over the disk is 58 to 34 K (percent bias reduction of 41%) at 160 km, 64 to 23 K (64%) at 215 km, 99 to 26 K (74%) at 300 km, and 113 to 33 K (71%) at 440 km. The mean of the ensemble spread (precision) of the measurement-updated estimate over the disk is 21 K at 160 km altitude, 32 K at 215 km, 40 K at 300 km, and 41 K at 440 km. These results correspond to an 18% , 24% , 27% , and 27% reduction in model uncertainty, respectively.

4.2. Storm Time OSSE

To demonstrate the effectiveness of the measurement-update during geomagnetically disturbed conditions, Figure 5 shows the results for the measurement-update during the peak response in the thermosphere to the geomagnetic disturbance at two atmospheric columns shown in Figure 6. The column in Figure 5a is located in the region with the most significant temperature changes and the column in Figure 5b is the same as Figure 3b. These two examples show the EnSRF can significantly reduce model bias given potentially large forecast biases in times of elevated forcing.

Figure 6 demonstrates the effects of the measurement-update over the disk at the same pressure levels shown in Figure 4. During the peak response in the thermosphere, the absolute mean temperature bias reduction from forecast to measurement-update over the disk is 102 K to 50 K (percent bias reduction of 51%) at 160 km, 147 to 46 K (69%) at 215 km, 217 to 66 K (70%) at 300 km, and 241 to 79 K (67%) at 440 km. These values correspond to a reduction in the absolute mean temperature bias over all grid points of 60% . The mean of the ensemble spread (precision) of the measurement-updated estimate over the disk is 20 K at 160 km altitude, 34 K at 215 km, 42 K at 300 km, and 43 K at 440 km. The total model uncertainty reduced by 28% from forecast to measurement-update. These are promising results, given known short-comings in current thermospheric models during times of increased magnetospheric forcing.

5. Discussion

5.1. Model Error

The estimation of vertical temperature structure from GOLD disk emission data is an under-determined inverse problem, requiring the use of prior information and/or regularization. The data assimilation approach presented in this paper uses the prior probability distribution of the temperature structure

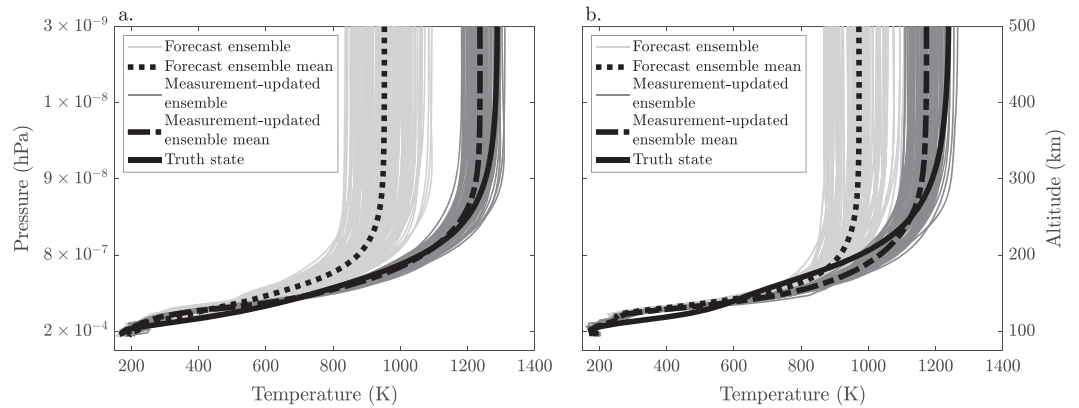


Figure 5. Example of temperature estimates in (a) the satellite's nadir direction and (b) near the limb during the thermosphere's peak response to the geomagnetic disturbance presented in the same manner as Figure 3. See the labeled pixels in Figure 6 for the location of these temperature profiles on the disk.

specified by the forecast model ensemble. According to Steps 2–4 of the EnSRF measurement update described in section 2.3, the measurement-updated temperature is computed by using the relationship between the GOLD disk emission and the temperature at each altitude level determined by two sets of ensemble: the forecast temperature ensemble $\{x_f^1, \dots, x_f^m\}$ and forecast observation ensemble $\{y_f^1, \dots, y_f^m\}$. The forecast temperature and observation ensembles are most correlated around 160–200 km depending on solar zenith angle, as the temperature in the lower thermosphere has the greatest contribution to LBH emissions observed by GOLD. The thermospheric temperature estimate depends on abilities of the forecast and forward models to realistically reproduce upper atmosphere physical processes at all the altitude ranges. It is important to identify the causes of model biases by analyzing patterns in the model-observation differences and comparing to independent observations from other ground-based and space-based instrumentations.

5.2. Observation

Specific forms of the GOLD observation assimilated in the EnSRF can be changed as long as the observation reflects temperature effects on the shape of the LBH features and is defined consistently with the forward model. A mean short to long spectral counts ratio was used as the observation for this study because it showed superior performance over other observation types tested including the total magnitude of LBH

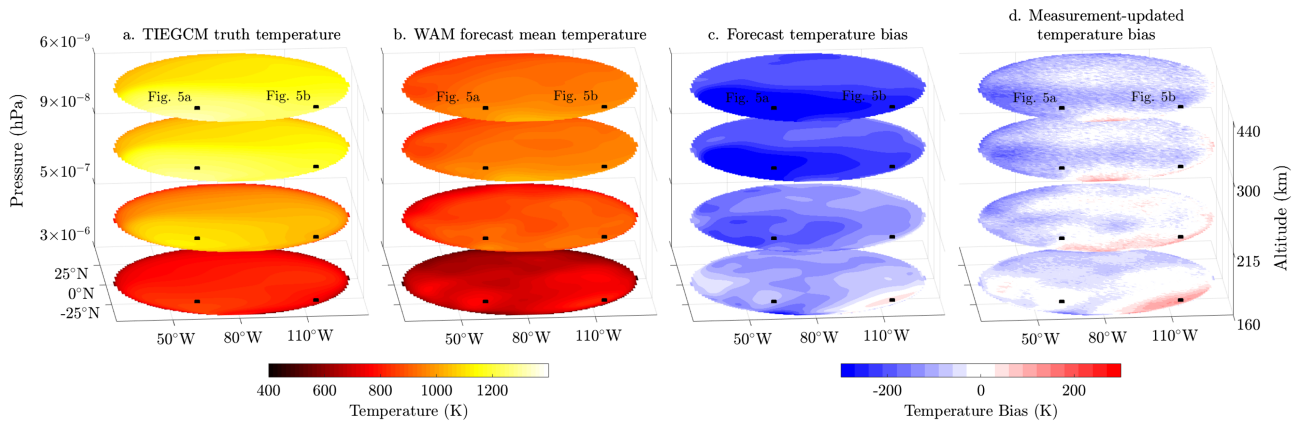


Figure 6. Three-dimensional plots during the thermosphere's peak response to the geomagnetic disturbance presented in the same manner as Figure 4. Compared to Figure 4, the color contour ranges have increased from 400–1200 K to 400–1400 K for (a) and (b) and from ± 200 to ± 300 for (c) and (d). Figure 5 shows a graphical representation of the measurement update for the labeled pixels.

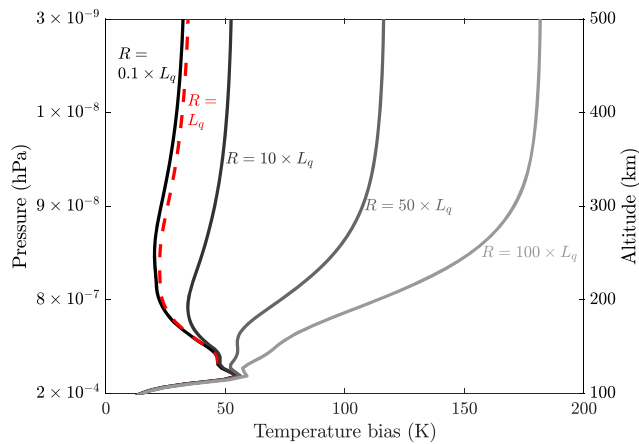


Figure 7. Absolute mean measurement-updated temperature bias over the disk for each WAM pressure level given varying values of observational error covariance, R . The dotted red line indicates the best estimate of R that is used in the case studies. L_q is the photon radiance. Counting statistics, expected to be the dominant noise source, are modeled as a Poisson distribution with mean and variance equal to or a multiple of L_q .

emission, the magnitude of individual features, and the magnitude of only the short or long counts of features. The first two observation types had the lowest performance because they did not reflect feature shape.

The use of short to long spectral counts ratio as the observation requires careful consideration for the spectral binning into short and long wavelength sections. This is because the peak of emission for a certain feature will shift to longer wavelengths as temperature increases. Shifting of the peak emission is well captured in the forward model in this study. We have accounted for this shifting by setting the short spectral bandwidth beyond the point of the peak of emission for the highest expected temperature. In the future, actual GOLD data will be used to define the ratio boundary.

5.3. Observation Error

The accuracy of the ensemble filter measurement-update is dependent on the representation of the observational error covariance, R , which defines the uncertainty in observations resulting from inadequacy in forward modeling as well as measurement and instrument noises. A lower uncertainty in observations results in a filter that trusts observations more than prior knowledge (forecast model). Figure 6 displays how the mean temperature bias over the disk changes with R at each altitude. These results

are obtained with recalibrated R to reflect different instrument noise characteristics that is represented by the Poisson distribution.

When R is at its current value or lower, the mean absolute measurement-updated temperature bias over the disk above 160 km altitude is <35 K with a minimum mean absolute bias of 23 K at ~215 km. If the observation error increases by a factor of ~10, the filter will still obtain reasonable accuracy with a mean measurement-updated temperature bias under 50 K throughout the thermosphere. This study was performed for 2012 conditions, and FUV photon counts are higher than present conditions in 2019. It is expected that given the lower photon counts in present-day and thus a lower signal-to-noise, the performance of the EnSRF will be closer to the $R = 10 \times L_q$ case shown in Figure 7. When GOLD Level 1C data is assimilated in the future, R must be adjusted to reflect both instrument performance determined after each recalibration analysis and uncertainties in the physics of the forward model. Furthermore, the effects of uncertainty in photo electron impact cross sections should be accounted for in modeling R .

Below 160 km, the mean bias increases with decreasing altitude up to 50 K at 110 km. Based on the observation error and model-observation biases, a new ensemble perturbation method may need to be adapted to represent the forecast covariance most appropriately to improve the performance of the EnSRF throughout the thermosphere. The ensemble used in this study is most sensitive to solar EUV variation based on the nature of its creation with perturbed solar EUV conditions. In the case of capturing lower atmosphere forcing variability, a new WAM ensemble perturbation method should consider a combination of perturbed solar and tropospheric conditions, which is likely to increase the sensitivity of the measurement-updated temperature at lower altitudes to observations.

6. Conclusions

An application of radiance data assimilation to the upper atmosphere is formulated by using a measurement-update step of the EnSRF. The OSSEs designed for GOLD FUV observations demonstrate the potential of the radiance data assimilation approach to estimate the three-dimensional structure of the thermosphere temperature from GOLD Level 1C disk data. The OSSEs showed that assimilation of the short to long wavelength ratio of LBH disk emission features into the WAM can reduce the model temperature biases from forecast to measurement update by 61% under geomagnetically quiet conditions and by 60% under disturbed conditions. The OSSEs also produced a reduction in model uncertainty as reflected by the ensemble spread of about 20% in the lower thermosphere and 30% in the upper thermosphere for both conditions. The ratio used in this study is one example of an observation type that helps accentuate the temperature effects on the shape

of LBH emission features. Selecting an optimal observation type will be important when assimilating actual GOLD data in the future.

Reconstruction of the three-dimensional temperature structure over the disk observed by GOLD is an exciting prospect to help understand the thermosphere's dynamic response to forcing from space and the lower atmosphere. The radiance data assimilation approach demonstrated in this paper presents opportunities to track transient features detected by GOLD data but absent in numerical models and improve modeled responses during times of elevated forcing. In the future, the implementation of EnSRF needs to be further refined by including a forecast step and using ensemble perturbations that encompass a full range of sources of the model uncertainty. This study is a first step to assimilate the GOLD disk image observations in a similar manner to lower atmosphere radiance data assimilation approaches. Incorporating this approach into existing whole atmosphere assimilation systems that are capable of assimilating a large variety of observations including the tropospheric and stratospheric observations will enable synthesis of GOLD data with other ground-based and satellite data for direct examination of the impact of lower atmosphere wave forcing in the thermosphere.

Acknowledgments

This work was supported by NASA award NNX14AI17G, NASA award 80NSSC19K1432, and NSF award AGS1848544. High-performance computing support from Cheyenne (doi:10.5065/D6RX99HX) was provided by the NCAR Computational and Information Systems Laboratory. NCAR is supported by cooperative agreement 1852977 from the National Science Foundation. We would like to thank Richard Eastes for sharing his knowledge of the GOLD instrument and the GOLD LBH temperature retrieval. Lastly, we would like to thank Dominic Fuller-Rowell for his early work in support of synthesizing WAM and GLOW. The main OSSE results presented in this paper are publicly available from doi:10.17605/OSF.IO/KMFZG.

References

- Akmaev, R. A. (2011). Whole atmosphere modeling: Connecting terrestrial and space weather. *Reviews of Geophysics*, 49, RG4004. <https://doi.org/10.1029/2011RG000364>
- Aksnes, A., Eastes, R., Budzien, S., & Dymond, K. (2006). Neutral temperatures in the lower thermosphere from N₂ Lyman-Birge-Hopfield (LBH) band profiles. *Geophysical Research Letters*, 33, L15103. <https://doi.org/10.1029/2006GL026255>
- Anderson, J. L. (2001). An ensemble adjustment Kalman filter for data assimilation. *Monthly Weather Review*, 129(12), 2884–2903.
- Anderson, J. L. (2003). A local least squares framework for ensemble filtering. *Monthly Weather Review*, 131, 634–642.
- Bishop, C. H., Etherton, B., & Majumdar, S. J. (2001). Adaptive sampling with the ensemble transform Kalman filter. Part I: Theoretical aspects. *Monthly Weather Review*, 129, 420–436.
- Budzien, S. A., Fortna, C. B., Dymond, K. F., Thonnard, S. E., Nicholas, A. C., McCoy, R. P., & Thomas, R. J. (2001). Thermospheric temperature derived from ARGOS observations of N₂ Lyman-Birge-Hopfield emission. 2001 AGUSM SA62A03B.
- Dymond, K. F., Wolfram, K. D., Budzien, S. A., Fortna, C. B., McCoy, R. P. (1999). High-resolution Ionospheric and Thermospheric Spectrograph (HITS) on the Advanced Research and Global Observing Satellite (ARGOS): quick look results, Proc. SPIE 3818, Ultraviolet Atmospheric and Space Remote Sensing: Methods and Instrumentation II.
- Eastes, R. W., McClintock, W. E., Burns, A. G., Anderson, D. N., Andersson, L., Codrescu, M., et al. (2017). The Global-Scale Observations of the Limb and Disk (GOLD) Mission. *Space Science Reviews*, 212(1-2), 383–408. <https://doi.org/10.1007/s11214-017-0392-2>
- Eastes, R. W., Murray, D. J., Aksnes, A., Budzien, S. A., Daniell, R. E., & Krywonos, A. (2011). Modeled and observed N₂ Lyman-Birge-Hopfield band emissions: A comparison. *Journal of Geophysical Research*, 116, A12308. <https://doi.org/10.1029/2010JA016417>
- Fang, T.-W., Akmaev, R., Fuller-Rowell, T. J., Wu, F., Maruyama, N., & Millward, G. (2013). Longitudinal and day-to-day variability in the ionosphere from lower atmosphere tidal forcing. *Geophysical Research Letters*, 40, 2523–2528. <https://doi.org/10.1002/grl.50550>
- Fang, T.-W., Fuller-Rowell, T. J., Yudin, V. A., Matsuo, T., & Viereck, R. (2018). Quantifying the sources of ionosphere day-to-day variability. *Journal of Geophysical Research: Space Physics*, 123, 9682–9696. <https://doi.org/10.1029/2018JA025525>
- Huber, K. P., & Herzberg, G. (1979). *Molecular Spectra and Molecular Structure IV. Constants of Diatomic Molecules*. Hoboken, N. J.: Van Nostrand Reinhold.
- Lean, J. L., & Blake, A. J. (1981). The effect of temperature on thermospheric molecular oxygen absorption in the Schumann-Runge continuum. *Journal of Geophysical Research*, 86(A1), 211–214. <https://doi.org/10.1029/JA086IA01P00211>
- Lee, I. T., Matsuo, T., Richmond, A. D., Liu, J. Y., Wang, W., Lin, C. H., et al. (2012). Assimilation of FORMOSAT-3/COSMIC electron density profiles into a coupled thermosphere/ionosphere model using ensemble Kalman filtering. *Journal of Geophysical Research*, 117, A10318. <https://doi.org/10.1029/2012JA017700>
- Lin, C. H., Hsiao, C. C., Liu, J. Y., & Liu, C. H. (2007). Longitudinal structure of the equatorial ionosphere: Time evolution of the four-peaked EIA structure. *Journal of Geophysical Research*, 112, A12305. <https://doi.org/10.1029/2007JA012455>
- Liu, H. L., Yudin, V. A., & Roble, R. G. (2013). Day-to-day ionospheric variability due to lower atmosphere perturbations. *Geophysical Research Letters*, 40, 665–670. <https://doi.org/10.1002/grl.50125>
- Matsuo, T., Fedrizzi, M., Fuller-Rowell, T. J., & Codrescu, M. V. (2012). Data assimilation of thermospheric mass density. *Space Weather*, 10, S05002. <https://doi.org/10.1029/2012SW000773>
- Meier, R. R., Picone, J. M., Drob, D., Bishop, J., Emmert, J. T., Lean, J. L., et al. (2015). Remote Sensing of Earth's Limb by TIMED/GUVI: Retrieval of thermospheric composition and temperature. *Earth and Space Science*, 2, 1–37. <https://doi.org/10.1002/2014EA000035>
- Paxton, L. J., Meng C.-I., Fountain, G. H., Ogorzalek, B. S., Darlington, E. H., Gary, S. A., et al. (1992). Special sensor ultraviolet spectrographic imager: an instrument description, Proc. SPIE 1745, Instrumentation for Planetary and Terrestrial Atmospheric Remote Sensing.
- Qian, L., Burns, A., Emery, B. A., Foster, B. T., Lu, G., Maute, A., et al. (2014). The NCAR TIE-GCM: A community model of the coupled thermosphere/ionosphere system. In J. Huba, R. Schunk, & G. Khazanov (Eds.), *Modeling the Ionosphere-Thermosphere System* (pp. 73–84). Washington: John Wiley & Sons. <https://doi.org/10.1002/9781118704417.ch7>
- Richmond, A. D., Ridley, E. C., & Roble, R. G. (1992). A thermosphere/ionosphere general circulation model with coupled electrodynamics. *Geophysical Research Letters*, 19, 601–604. <https://doi.org/10.1029/92GL00401>
- Solomon, S. C. (2017). Global modeling of thermospheric airglow in the far-ultraviolet. *Journal of Geophysical Research: Space Physics*, 122, 7834–7848. <https://doi.org/10.1002/2017JA024314>
- Solomon, S. C., & Qian, L. (2005). Solar extreme-ultraviolet irradiance for general circulation models. *Journal of Geophysical Research*, 110, A10306. <https://doi.org/10.1029/2005JA011160>

- Tippett, M. K., Anderson, J. L., Bishop, C. H., Hamill, T. M., & Whitaker, J. S. (2003). Ensemble square root filters. *Monthly Weather Review*, *131*(7), 1485–1490. [https://doi.org/10.1175/1520-0493\(2003\)131<1485:ESRF>2.0.CO;2](https://doi.org/10.1175/1520-0493(2003)131<1485:ESRF>2.0.CO;2)
- Torr, M. R., Torr, D. G., Zukic, M., Johnson, R. B., Ajello, J., Banks, P., et al. (1995). A far ultraviolet imager for the International Solar-Terrestrial Physics Mission. *Space Science Reviews*, *71*(1-4), 329–383. <https://doi.org/10.1007/BF00751335>
- Whitaker, J., & Hamill, T. M. (2002). Ensemble data assimilation without perturbed observations. *Monthly Weather Review*, *130*, 1913–1924.
- Whitaker, J. S., Hamill, T. M., Wei, X., Song, Y., & Toth, Z. (2008). Ensemble data assimilation with the NCEP Global Forecast System. *Monthly Weather Review*, *136*, 463–482.